Nanoscale

View Online
Dynamic Article Links

Cite this: *Nanoscale*, 2011, **3**, 265

www.rsc.org/nanoscale

PAPER

The kinetics and mechanisms of amorphous calcium carbonate (ACC) crystallization to calcite, *via* vaterite.

Juan Diego Rodriguez-Blanco,* Samuel Shaw and Liane G. Benning

Received 13th August 2010, Accepted 6th October 2010
DOI: 10.1039/c0nr00589d

The kinetics and mechanisms of nanoparticulate amorphous calcium carbonate (ACC) crystallization to calcite, *via* vaterite, were studied at a range of environmentally relevant temperatures (7.5–25 °C) using synchrotron-based *in situ* time-resolved Energy Dispersive X-ray Diffraction (ED-XRD) in conjunction with high-resolution electron microscopy, *ex situ* X-ray diffraction and infrared spectroscopy. The crystallization process occurs in two stages; firstly, the particles of ACC rapidly dehydrate and crystallize to form individual particles of vaterite; secondly, the vaterite transforms to calcite *via* a dissolution and reprecipitation mechanism with the reaction rate controlled by the surface area of calcite. The second stage of the reaction is approximately 10 times slower than the first. Activation energies of calcite nucleation and crystallization are 73 ± 10 and 66 ± 2 kJ mol^{-1}, respectively. A model to calculate the degree of calcite crystallization from ACC at environmentally relevant temperatures (7.5–40 °C) is also presented.

Introduction

The abiotic and biogenic formation of calcium carbonate minerals (*e.g.* calcite) occurs in a wide range of natural environments (*e.g.* soils and calcifying marine plankton), and is a key component of the global carbon cycle.[1] The formation of crystalline calcium carbonate polymorphs (calcite, vaterite and aragonite) during biomineralization often occurs *via* a nanoparticulate Amorphous Calcium Carbonate (ACC) precursor.[2] The crystallization of ACC to calcite enables organisms to form biominerals with complex morphologies and crystals with defined crystallographic orientations. For example, sea urchin spines consist of a single crystal of calcite with the c-axis aligned parallel to the length of the spicules.[3] The intricate shape of these biominerals is achieved by the initial deposition of ACC nanoparticles, which then spontaneously crystallize to form a spine composed of a single calcite crystal. In recent years these biomineralisation processes have stimulated significant interest due to their potential to be mimicked and applied to form industrial products with specific particle shapes.[4] Also, these calcium carbonate transitions can be utilized to incorporate proteins (*e.g.* insulin) into the final crystalline phase for potential drug delivery applications.[5] However, the nanoscale mechanisms of the calcium carbonate crystallization pathways are still poorly defined. Furthermore, there are currently no quantitative kinetic models to describe the transformation from ACC to crystalline calcite at ambient conditions. This is despite the fact that such information is crucial for understanding the physical and chemical conditions which lead to calcium carbonate biomineralisation or the production of particles with specific shape/size for industrial applications.[6]

Recent studies have shown that the chemical composition of ACC is nominally $CaCO_3 \cdot H_2O$.[7] The ACC structure consists of a calcium-rich nanoscale framework with pores containing water and carbonate ions. The pores are approximately 1 nm in diameter and interconnect to form channels which run through the particles of ACC. ACC is thermodynamically unstable, and will spontaneously crystallize when suspended in an aqueous solution at ambient temperatures. This process is rapid (minutes to hours) and leads to the formation of calcite, aragonite and/or vaterite depending on the physical and chemical conditions. Pure ACC (non-additives) will transform to calcite *via* a vaterite intermediate at low temperatures (<30 °C) and to aragonite *via* vaterite at higher temperatures (≥40 °C).[8,9] Impurities substituted into ACC can also influence the crystallisation pathway, with the addition of magnesium leading to the crystallisation of calcite, with no vaterite intermediate.[9–11] Ogino *et al.* (1987)[9] used measurements of solution chemistry and X-ray diffraction to characterize the pure ACC formation and transformation. Their data indicate that the initial ACC precipitated rapidly and transformed to vaterite within minutes. The vaterite in turn transformed to calcite *via* a dissolution-reprecipitation mechanism. Kinetic studies of this second crystallization step at elevated temperatures (25–80 °C) using mixtures of vaterite and calcite seeds[12] suggested that calcite growth was the rate determining step.

Currently, there is a lack of kinetic and mechanistic information on the crystallization of ACC at temperatures equivalent to those where biomineralization occurs in the natural environment

School of Earth and Environment, University of Leeds, Leeds, LS2 9JT, United Kingdom. E-mail: j.d.rodriguez@see.leeds.ac.uk

(<25 °C). This is primarily because no study has systematically analyzed the complete transformation from precipitation of ACC to calcite, *via* vaterite. Furthermore, most studies have only characterized individual components of this crystallization reaction (*e.g.* vaterite to calcite[12]) and were performed using *ex situ* analyses with relatively low temporal resolutions (from 10's of minutes to 10's of hours). In this study we have used *in situ* synchrotron-based Energy Dispersive X-ray diffraction (ED-XRD) at a high temporal resolution (<1 min) in conjunction with high-resolution electron microscopy and infrared spectroscopy to characterize ACC formation and its crystallisation to calcite, *via* vaterite. This data provides a detailed mechanistic insight into the transformation mechanisms of both ACC to vaterite and vaterite to calcite. Also, the time-resolved diffraction data has been used to derive a model for the formation of calcite from ACC at temperatures relevant to biomineralization and industrial synthesis processes.

Experimental methods

$CaCO_3$ crystallization experiments were carried out by mixing thermally equilibrated 1M Na_2CO_3 and $CaCl_2$ solutions (CO_3^{2-}:Ca^{2+} = 1 : 1 ratio) in an 80 mL thermostated and stirred Teflon® reaction cell. The experiments were performed at 7.5, 10, 20 and 25 °C, and the reactions were followed *in situ* using time resolved ED-XRD. These experiments were performed on station 16.4 at the Synchrotron Radiation Source, Daresbury Laboratory, U.K. A detailed description of the ED-XRD experimental protocol and data processing can be found in Shaw *et al.* (2005)[13] and Davidson *et al.* (2008).[14] Depending on temperature, ED-XRD patterns of the reaction cell contents were recorded at time intervals between 15 s and 1 min, and reactions were followed for a maximum of 20 h. The first appearance of a diffraction peak represented the start of the crystallization reactions (induction time), while the reactions were considered complete when no further changes in the intensities of the diffraction peaks were observed. The individual ED-XRD patterns were fitted using XFIT[15] and the peak areas as a function of time were calculated and normalized to values from 0 to 1 to express the degree of reactions (α).

Experiments analogous to those performed on-line were undertaken off-line in order to obtain samples for solid characterization at various time intervals during the crystallization reaction. The solids precipitated immediately after mixing were quenched by vacuum-filtration (0.2 μm polycarbonate filters) and washed with isopropanol following the procedure described in Rodriguez-Blanco *et al.* (2008).[16] The remaining solid phases (>30 s after mixing, *i.e.* intermediate phases and end-products) were separated from the aqueous solutions by centrifugation and filtration after which they were washed with isopropanol and dried at 25 °C in an oven. All off-line solids were characterized with a Bruker D8 powder X-ray diffractometer with a Ge(111) monochromator, (Cu-Kα_1 = 1.54 Å; 2θ = 5–70° range; patterns recorded at 0.001° steps at 0.5 s/step) for their mineralogical composition. XRD patterns of the poorly ordered samples obtained immediately after mixing (1–30 s) were recorded at a slower scan rate (2 s/step) in order to improve the clarity of the low intensity diffraction peaks.

Fourier transform infrared spectra (FTIR) were acquired over the mid infrared region (650 to 4000 cm^{-1}) using an A2-Technology MicroLab Portable mid-IR spectrometer, with a diamond internal reflection (DATR). Spectra were accumulated by co-adding 512 scans with a 4 cm^{-1} resolution and spectral manipulation including baseline adjustment, smoothing, normalization, and band component analysis was carried out using the Thermo Nicolet OMNIC ESP 5.1 software package.

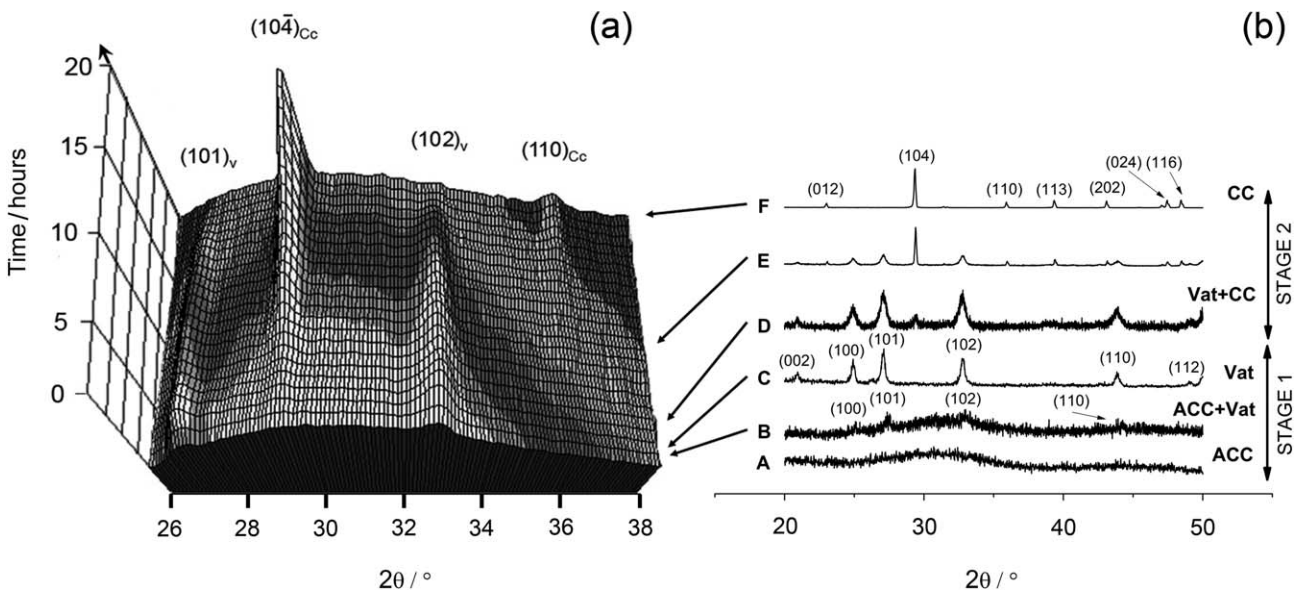

Fig. 1 (a) Three-dimensional representation of time-resolved ED-XRD patterns showing the evolution of vaterite (101), (102) and calcite (104) and (110) reflections at 7.5 °C. Energy has been converted to 2θ using the Bragg equation (2dsinθ = nλ) and assuming λ = 1.541 Å for Cu-Kα. (b) X-ray diffraction patterns of solids collected at different elapsed times during the off-line experiments, showing ACC, vaterite and calcite solid phases.

High resolution images of the solids were acquired using a Field Emission Gun Scanning Electron Microscope (FEG-SEM, LEO 1530 Gemini at 3KeV).

Finally, the saturation indexes (SI) for the different solid phases and their Ion Activity Products (IAP) were calculated with the geochemical code PHREEQC, using the initial solution composition and the solubility products for ACC[17] and $CaCO_3$ polymorphs[18] as integrated in the wateq4f database.[19]

Results and discussion

Diffraction data collected *in situ* and *ex-situ* for the crystallization of ACC at 7.5 °C showing a representative crystallization pathway are presented in Fig. 1. The 3D plot (Fig. 1a) shows the time-resolved ED-XRD patterns while the conventional XRD patterns (Fig., 1b) were collected from five samples obtained at different elapsed times (A–F) in an identical *ex-situ* experiment.

Immediately upon mixing the starting solutions, a gel-like white precipitate formed. This initial precipitate exhibited no distinct diffraction peaks in the ED-XRD patterns and revealed only a broad hump derived from the combined scattering from the poorly-ordered precipitate and the aqueous solution. The off-line XRD patterns (pattern A in Fig. 1b) confirmed that this initial precipitate consisted of a poorly-ordered material, with two broad humps at approximately 30° and 45° 2θ which are characteristic of ACC.[16] FTIR spectra of this initial phase (Fig. 2, bottom pattern) were characterized by a broad band between 2700 and 3600 cm^{-1} (O–H stretching) and a shaper band at 1650 cm^{-1} (O–H bending), both of which correspond to structural water within ACC (water contents can reach up to 18wt%).[20] In addition, ACC was also confirmed by the presence of a shoulder on the main asymmetric ν_3 CO_3 band (at 1460 cm^{-1})[21] and the absence of the ν_4 symmetric vibration at 725 cm^{-1}. This latter vibration is characteristic of crystalline calcium carbonate phases only (upper pattern in Fig. 2). The remaining bands representing the vibrations of the carbonate ions (1805, 1409, 1090 and 874 cm^{-1})[22] are common in both poorly-ordered ACC and crystalline polymorphs.

As the reaction progressed the ED-XRD patterns revealed that the broad hump started decreasing and after a temperature-dependent induction time the vaterite (101) and (102) peaks started growing (Fig. 1a). These peaks rapidly increased in intensity as vaterite crystallized until they reached a maximum (*e.g.*, at 7.5 °C after ~1 h; see Fig. 3). Once a maximum was reached the vaterite peak intensities started to decrease and this was mirrored by the growth of the calcite (104) and (110) peaks. Calcite was the sole crystalline phase at the end of all experiments. This crystallization pathway was observed in all experiments and in all cases the crystallization reaction followed a two-stage process. In a first stage, the initially precipitated ACC crystallized to the intermediate calcium carbonate polymorph vaterite. The second stage of the transformation reaction was controlled by the crystallization of vaterite to calcite. The relative time length of the two-stage crystallization pathway is clearly observed when the changes in the degree of reaction for vaterite and calcite for an experiment are presented as a function of time (*e.g.* 7.5 °C, Fig. 3).

SEM photomicrographs of the solids from stage 1 (Fig. 4a–e) revealed that the ACC obtained immediately after mixing consisted of nanoparticles <50 nm in diameter with roughly spherical shape and low polydispersity (Fig. 4-a). The vaterite, which crystallized after ACC, formed large aggregates (<500 nm, Fig. 4-b). These vaterite aggregates consisted of nanoparticles with similar dimensions to the nanoparticulate ACC (Fig. 4-c). These vaterite spheres coexisted for a brief period (<15 min at 7.5 °C) with the precursor ACC nanoparticles. As the reaction progressed, the poorly-ordered ACC fully disappeared and only the micron-sized vaterite aggregates remained (Fig. 4-d,e). In stage 2, as the crystallization progressed the amount of vaterite decreased and calcite crystals formed on the surface of the vaterite aggregates (Fig. 4f-g, corresponding to XRD patterns D and E in Fig. 1b). During the final stages of calcite growth, the amount of vaterite progressively decreased until only individual nanoparticulate subunits (<50 nm) (Fig. 4-h) were present on the surface of the newly formed calcite crystals. The final end product, calcite, consisted of euhedral and subhedral crystals, which frequently showed pseudospherical casts after vaterite

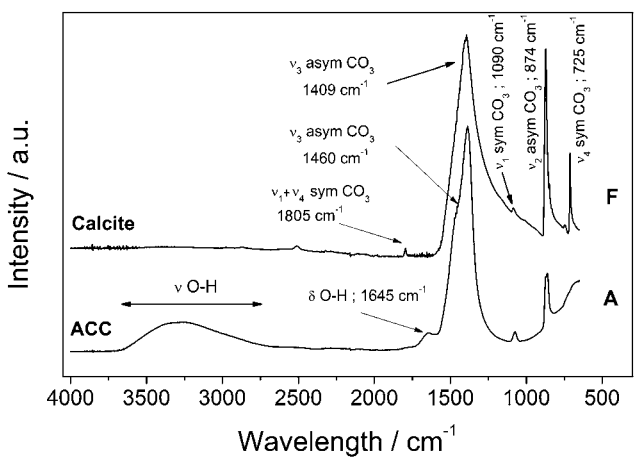

Fig. 2 Fourier Transform Infrared (FTIR) spectra of ACC and calcite showing the change in water content from the amorphous hydrated precursor and the non-hydrated crystalline calcium carbonate phases. 'A' and 'F' represent the same samples shown in the XRD patterns (Fig. 1).

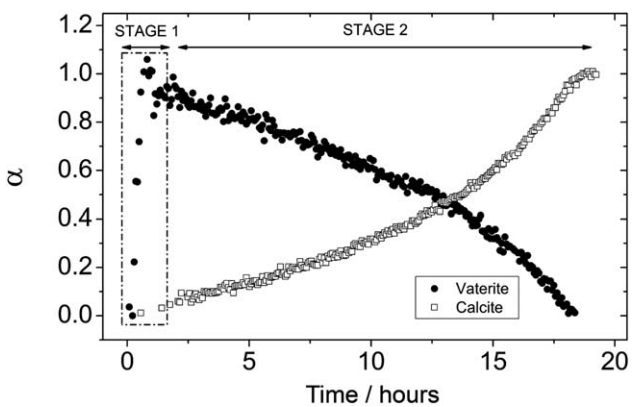

Fig. 3 Degree of reaction (α) determined from the dissolution of vaterite (101) and growth of calcite (104) reflections as a function of time at 7.5 °C. The ACC-vaterite and vaterite-calcite transformations are differentiated as stages 1 and 2, respectively.

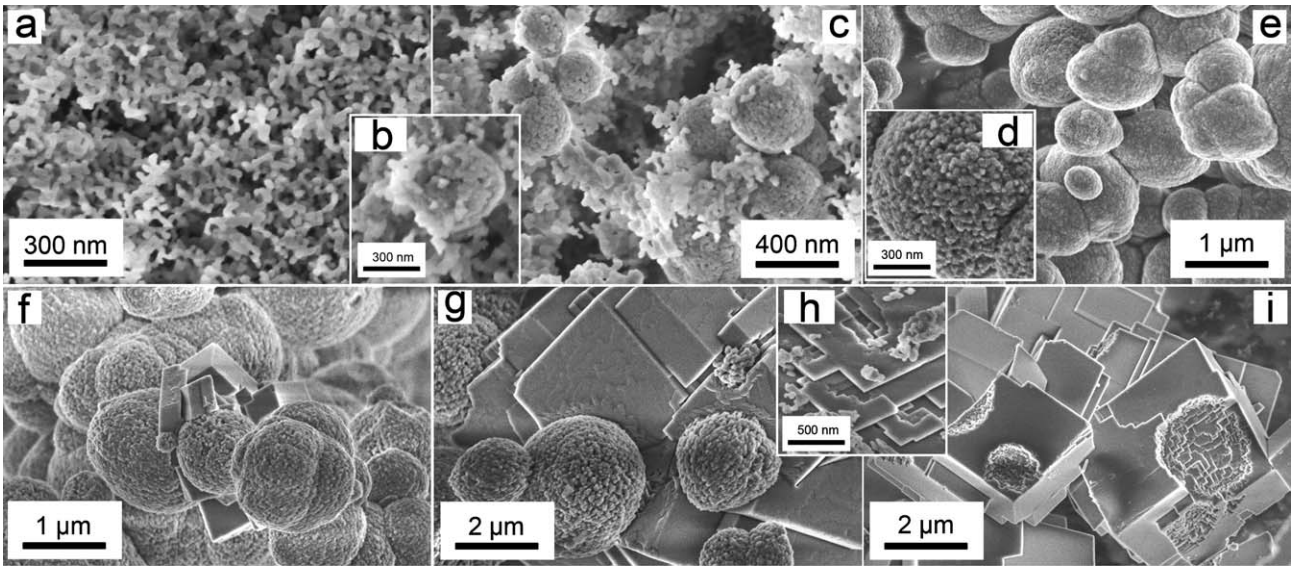

Fig. 4 FEG-SEM images of the solid phases which form during the two stages of the crystallization experiments. Pictures on the top correspond to Stage 1, showing amorphous calcium carbonate (ACC, a); ACC and vaterite nanoaggregates (b, c); and vaterite nanoaggregates (d, e). Pictures at the bottom correspond to Stage 2: vaterite nanoaggregates and first calcite crystals (f); calcite crystals attached to vaterite spheres with the development of growth steps on the calcite surface (g); calcite growth steps and vaterite nanoparticulate subunits (h) and calcite crystals with vaterite casts (i).

(Fig. 4-i). These casts were a product of the calcite forming on and around the spherical aggregates of vaterite.

Stage 1: amorphous calcium carbonate (ACC) to vaterite transformation

We have quantitatively evaluated the crystallization of ACC to vaterite using the time-resolved XRD spectra and derived a mechanistic understanding of the initial crystallization step. During the crystallization the background intensity in the ED-XRD patterns in a 2θ range where no diffraction peaks were observed decreased, while in tandem vaterite peaks started growing (Fig. 5, experiment at 7.5 °C). The decrease in the background intensity shows that the breakdown of ACC is coupled to the growth of the vaterite (101) peak area.

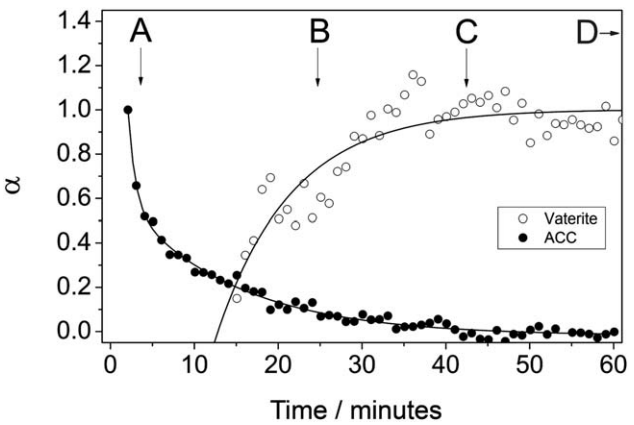

Fig. 5 Degree of reaction (α) determined from the vaterite (101) peak area and from the ED-XRD background intensity at 7.5 °C. Characters A to D represent the samples taken from the off-line experiments after specific elapsed times which are also correlated with XRD (Fig. 1b) and FTIR (Fig. 2).

Interestingly however, the decrease in the background intensity started before the first vaterite peaks were observed (*e.g.*, at 7.5 °C, vaterite peaks started growing 14 min after the initial decrease in the ACC). This transformation was observed at all temperatures and this stage of the crystallization process occurred at a faster rate at higher temperatures. For example, at 7.5 °C ACC breakdown was complete after ~45 min coinciding with the full vaterite growth (Fig. 5), while at 25 °C the ACC breakdown was complete and vaterite was fully grown after 12 min. The coupled ACC breakdown and vaterite growth observed with ED-XRD clearly matches with the SEM observations, which show the coexistence of ACC and vaterite during a short (<15 min at 7.5 °C) time interval (Fig. 4 b–c).

Combining information from the diffraction, electron microscopy and infrared spectroscopy, the key structural and physical processes which control the ACC to vaterite crystallization can be derived; firstly, the SEM images show that vaterite consists of aggregated nanoparticle sub-units which were smaller in average size (~30 to 70 nm) than the primary ACC particles (~20 to 45 nm) (Fig. 4). Secondly, the loss of the water as revealed by FTIR indicates that ACC dehydrated during its transformation into crystalline $CaCO_3$ (Fig. 2). Thus, we infer that the transformation of ACC to vaterite is due to the rapid dehydration of the ACC structure followed by an internal structural reorganisation within the individual nanoparticles to form vaterite. The reduction of the XRD background intensity prior to the formation of vaterite may be due to initial dehydration and local ordering of the ACC structure prior to the formation of crystalline vaterite. This crystallization mechanism is supported by the recent work of Goodwin *et al.* (2010),[7] who suggested that the local coordination environment of Ca in the nanoframework structure of ACC is similar to those in crystalline $CaCO_3$ phases (*e.g.* vaterite and calcite). Therefore the dehydration and condensation of the ACC structure could lead to the formation of vaterite without major structural

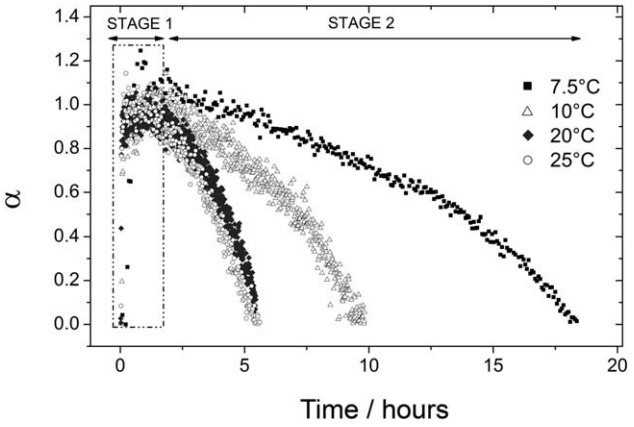

Fig. 6 Degree of reaction (α) determined from the dissolution of vaterite (101) reflection as a function of time at four different temperatures (7.5 to 25 °C).

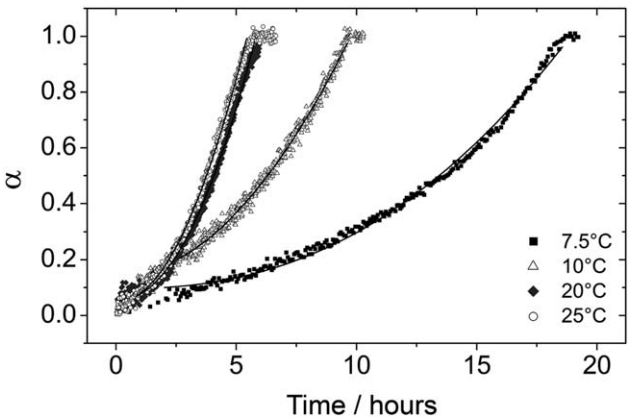

Fig. 7 Degree of reaction (α) determined from the growth of calcite (104) reflection as a function of time at four different temperatures (7.5 to 25 °C). The fitting curves using eqn (1) from Ogino *et al.*, (1990)[12] kinetic model are also shown as solid lines for all the plots.

rearrangements. This mechanism is supported by the small change in particle size, which suggests that the individual ACC nanoparticles have indeed transformed to vaterite. Furthermore, the lack of defined crystal faces on the vaterite sub-units (Fig. 4-d) suggests they have not formed by controlled precipitation from solution, which usually leads to particles with a defined crystalline morphology. All these lines of evidence and observations suggest that the formation of vaterite is controlled by the breakdown of ACC and that this transformation occurs *via* a progressive dehydration of the ACC combined with aggregation and crystallization of ACC to form vaterite.

Stage 2: vaterite-calcite transformation

During the second stage of the reaction vaterite crystallized to calcite. The solubility of the $CaCO_3$ polymorphs is the key factor controlling growth of calcite during this stage.[9] When vaterite is present the composition of the solution will be controlled by the solubility of this phase, as the solubility of vaterite (K_{sp} $10^{-7.913}$) is greater than that of calcite (K_{sp} $10^{-8.480}$).[18] Therefore the solution will remain supersaturated with respect to calcite driving the precipitation of this phase.

The changes in vaterite and calcite diffraction peak areas at all temperatures evaluated here during stage 2 are presented in Fig. 6 and 7. The data show that the rate of both the vaterite breakdown and calcite growth increase with time. Ogino *et al.* (1990)[12] suggested, in seeded experiments, that the transformation of vaterite to calcite was dependent of the surface area of calcite present. In the current study, as the reaction progresses the amount of newly formed calcite surface also increases and thus the rate of reaction increases as the transformation occurs. This indicates that the vaterite dissolves releasing calcium and carbonate into solution, which then reprecipitate on the surface of the growing calcite crystals. This mechanism is supported by the SEM observations (Fig. 4), which clearly show the calcite crystals growing on the surface of the vaterite aggregates. In addition, the spherical casts still evident in the final calcite crystals (Fig. 4-i) suggest that the dissolution of vaterite and the precipitation of calcite are separate processes, further supporting the hypothesis that the transformation of vaterite to calcite is not a solid-state transformation but a surface-controlled process.

The calcite diffraction peak area growth as a function of time was fitted using the kinetic model developed by Ogino *et al.* (1990),[12] which has been used to define the formation of calcite from vaterite in seeded systems:

$$\alpha = (b(t - t_0) + c)^3 \quad (1)$$

where

$$b = kf_x A_0^{\frac{2}{3}} \frac{s_0}{3} \quad (2)$$

where c is an integration constant, t is time (seconds), t_0 is the induction time (seconds), k (s^{-1}) is the rate constant for calcite growth, and A_0 and s_0 are the amount of seed (moles) and surface area (m^2) of calcite at the beginning of the transformation, respectively. f_x is a term related to the supersaturation ratio of the solution with respect to calcite[23] and is given by:

$$f_x = [(IAP)^{1/2} - (K_{sp})^{1/2}] \quad (3)$$

where K_{sp} is the solubility product for calcite at a given temperature and IAP is the ion activity product of the solution. During the transformation from vaterite to calcite it can be assumed that the solution is saturated with respect to vaterite, therefore the IAP of the solution can be calculated from the solubility product of vaterite at a given temperature.

The kinetic model (1) was fitted to the diffraction data for calcite formation at 25 °C to derive values for b and c (Table 1). A_0 was taken to be the value of α at t_0 (*i.e.* when vaterite starts to breakdown). s_0 could then be calculated by substituting the rate constant for calcite formation at 25 °C (2.67×10^2 s^{-1}) from Ogino *et al.* (1990)[12] into eqn (2), which produced a value of 0.188 m^2. If it is assumed that the density of calcite is 2.71g cm^{-3} and that the crystals of calcite are rhombohedral in shape, which was confirmed by the SEM images (Fig. 4), the particle size of calcite at t_0 can be calculated to be 0.63 μm. This estimate is consistent with the SEM images of the initial calcite crystal size formed during the transformation which are between 0.5 and

Table 1 Results of the kinetic analysis of the ED-XRD data for the growth of calcite (104) peak. Results have been derived from our experiments and Ogino *et al.*, (1990)[12] data

Calcite crystallization					
T/°C	Induction time/s	k ($\cdot 10^2$ s^{-1}) (this study)	k ($\cdot 10^2$ s^{-1})[12]	b ($\cdot 10^{-6}$)	c
7.5	5100	0.71(0)		2.10(1)	0.0805(5)
10	2880	0.86(0)		3.52(1)	0.1013(4)
20	936	2.19(0)		7.18(2)	0.0719(4)
25	792	2.67[a]	2.67	7.66(4)	0.0724(5)
30			4.67		
40			11.0		
50			28.3		
60			58.3		
$Ea_{(nucl)}$ (KJ/mol)		73(10)			
$lnA_{(nucl)}$ (s^{-1})		23(4)			
$Ea_{(cryst)}$ (KJ/mol)		66(2)			
$lnA_{(cryst)}$ (s^{-1})		32(1)			

[a] Data has been fixed to match with Ogino *et al.* (1990) in order to calculate the initial particle size of calcite.

1 μm (Fig. 4-f). This particle size was then used to calculate s_0 at all temperatures using the measured values of A_0, assuming rhombohedral particle shape and the density of calcite. Following this the rate constant for calcite growth (k) was calculated at each temperature.

Rate constants (k), induction times (t_0) and the b and c parameters for the growth of calcite at all temperatures are shown in Table 1. The derived induction times and rate constants as a function of temperature were used to calculate apparent activation energies for nucleation ($Ea_{(nucl.)}$) and crystallization ($Ea_{(cryst.)}$) for calcite using an Arrhenius approach[13] (Table 1 and Fig. 8). The data on the Arrhenius plot describing calcite growth shows an excellent linear correlation ($R^2 > 0.99$) between the rates from this study and those from Ogino *et al.* (1990),[12] indicating that the data from these two studies can be combined. The derived $Ea_{(cryst.)}$ value for calcite growth using the data from both studies is 66 ± 2 kJ mol^{-1}. This activation energy for calcite formation is within the range suggested for surface-controlled reactions (<34 kJ mol^{-1}).[24] Also, several other authors have derived activation energies for seeded calcite growth ranging from ~39 to ~70 kJ mol^{-1},[25–28] which are similar to the value derived in this study.

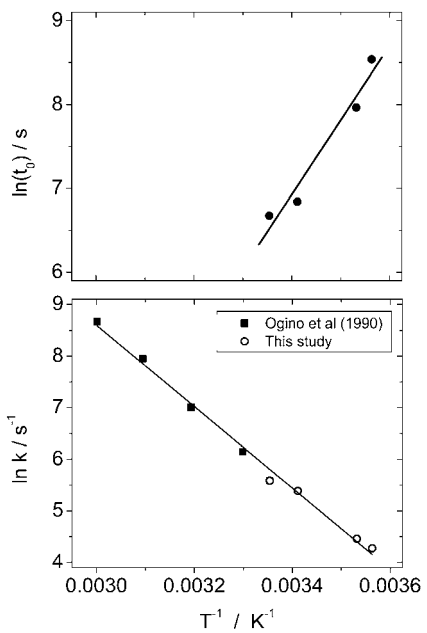

Fig. 8 Arrhenius plots for calcite nucleation (top) and crystallization (bottom). Kinetic data from Ogino *et al.* (1990)[12] is included in the latter.

An equation to model the degree of calcite crystallization from ACC at any given temperature can be derived by the rearrangement of eqn (1) and incorporating the rearranged Arrhenius equation for induction time (t_0) as a function of temperature. This produces a model for the degree of calcite formation (α) as a function of time at a range of temperatures:

$$t = e^{(-23.2+8862T^{-1})} + \frac{\sqrt[3]{\alpha - c}}{b} \quad (4)$$

Where t is time in seconds and T is temperature in K, α is the degree of calcite crystallization, and b and c are the coefficients given in Table 1. This equation can be use to model calcite crystallization from pure ACC at temperatures less than 30 °C, as crystallization at higher temperatures (≥40 °C) leads to the formation of aragonite.[8,9] Using this model indicates that the complete transformation of pure ACC to calcite occurs on a time scale of between ≈4–16 h at temperatures equivalent to those found in the natural environment (*e.g.* marine conditions). Beniash *et al.* (1997)[3] showed that ACC in sea urchin larval spicules crystallizes to calcite with time. They showed an increase in the proportion of calcite within an individual spicule over a number of days. This rate of transformation is clearly longer than would be predicted from the data in this study, and no evidence for vaterite has been observed in sea urchin spicules. The reason for these discrepancies may be due to presence of magnesium (≈5%) or organic matter in the biomineralised $CaCO_3$,[3] which are known to reduce the rate of calcite growth, and stabilize calcite over vaterite.[29] However, the proposed model could be used to determine the rate of calcite formation in pure biomineralised $CaCO_3$.

Conclusions

This is the first complete study of the kinetics and mechanisms of the two-stage crystallization pathway of ACC to calcite at a range of ambient temperatures using high temporal resolution *in situ* and time-resolved analysis. Our data revealed that the first stage of crystallization proceeded *via* the dehydration of the initial ACC to form nanocrystalline vaterite. This is followed by a slower second stage which is a surface-controlled process driven by the growth of the calcite. This formation pathway has relevant implications for biomineralization and industrial calcium carbonate formation.

Acknowledgements

This research was supported by the Marie Curie EU-FP6 MINGRO Research and Training Network under contract MRTN-CT-2006-035488 and the CCLRC grants for beamtime (50115 and 50218 to Liane G. Benning). The authors would also like to thank Dr Dave Taylor from the Synchrotron Radiation Source, Daresbury Laboratory, UK for help during beamtime and our colleagues Miss Gabriella Kakonyi and Dr Vu Hong Phuc for help during the experimental work and data evaluation.

References

1 R. Reeder., *Reviews in Mineralogy*, Mineralogical Society of America, Washington, D.C., 1983, vol. 11, 394 pp.
2 S. Weiner, I. Sagi and L. Addadi, *Science*, 2005, **309**, 1027–1028.
3 E. Beniash, J. Aizenberg, L. Addadi and S. Weiner, *Proc. R. Soc. London, Ser. B*, 1997, **264**, 461–465.
4 F. C. Meldrum and S. Ludwigs, *Macromol. Biosci.*, 2007, **7**, 152–162.
5 M. Fujiwara, K. Shiokawa, M. Araki, N. Ashitaka, K. Morigaki, T. Kubota and Y. Nakahara, *Cryst. Growth Des.*, 2010, **10**, 4030, DOI: 10.1021/cg100631v.
6 F. C. Meldrum and H. Cölfen, *Chem. Rev.*, 2008, **108**, 4332–4432.
7 A. L. Goodwin, F. M. Michel, B. L. Phillips, D. A. Keen, M. T. Dove and R. J. Reeder, *Chem. Mater.*, 2010, **22**, 3197–3205.
8 J. L. Wray and F. Daniels, *J. Am. Chem. Soc.*, 1957, **79**, 2031–2034.
9 T. Ogino, T. Suzuki and K. Sawada, *Geochim. Cosmochim. Acta*, 1987, **51**, 2757–2767.
10 K. Sawada, *Pure Appl. Chem.*, 1997, **69**, 921–928.
11 J. D. Rodriguez-Blanco, P. Bots, N. J. Terrill, S. Shaw and L. G. Benning, *Geochim. Cosmochim. Acta*, 2010, **74**, 876.
12 T. Ogino, T. Suzuki and K. Sawada, *J. Cryst. Growth*, 1990, **100**, 159–167.
13 S. Shaw, S. E. Pepper, N. D. Bryan and F. R. Livens, *Am. Mineral.*, 2005, **90**, 1852–1860.
14 L. E. Davidson, S. Shaw and L. G. Benning, *Am. Mineral.*, 2008, **93**, 1326–1337.
15 R. W. Cheary and A. Coelho, *J. Appl. Crystallogr.*, 1992, **25**, 109–121.
16 J. D. Rodriguez-Blanco, S. Shaw and L. G. Benning, *Mineral. Mag.*, 2008, **72**, 283–286.
17 L. Brečević and A. E. Nielsen, *J. Cryst. Growth*, 1989, **98**, 504–510.
18 L. N. Plummer and E. Busenberg, *Geochim. Cosmochim. Acta*, 1982, **46**, 1011–1040.
19 J. W. Ball and D. K. Nordstrom., *U.S. Geological Survey Open-File Report*, 1991, 90–129, 185 p.
20 S. H. Huang, K. Naka and Y. Chujo, *Langmuir*, 2007, **23**, 12086–12095.
21 X. Wang, R. Kong, X. Pan, H. Xu, D. Xia, H. Shan and J. R. Lu, *J. Phys. Chem. B*, 2009, **113**, 8975–8982.
22 F. A. Andersen and L. Brečević, *Acta Chem. Scand.*, 1991, **45**, 1018–1024.
23 G. H. Nancollas and K. Sawada, *J. Petrol. Technol.*, 1982, **34**, 645–652.
24 A. C. Lasaga., in *Kinetic Theory in the Earth Sciences*. Princeton University Press, Princeton, New Jersey, 1998, 811 pp.
25 T. F. Kazmierczak, M. B. Tomson and G. H. Nancollas, *J. Phys. Chem.*, 1982, **86**, 103–107.
26 A. Gutjahr, H. Dabringhaus and R. Lacmann, *J. Cryst. Growth*, 1996, **158**, 296–309.
27 G. H. Nancollas and M. N. Reddy, *J. Colloid Interface Sci.*, 1971, **37**, 824–830.
28 D. Kralj, L. Brečević and J. Kontrec, *J. Cryst. Growth*, 1997, **177**, 248–257.
29 K. J. Davis, P. M. Dove and J. J. De Yoreo, *Science*, 2000, **290**, 1134–1137.